Methodology and Insights for System Calibration in Multi-angle Illumination Imaging

Thesis by
Catherine Deng

In Partial Fulfillment of the Requirements for the
Degree of
Bachelor of Science, EE

Caltech

CALIFORNIA INSTITUTE OF TECHNOLOGY
Pasadena, California

10 June 2025

ACKNOWLEDGEMENTS

[Add acknowledgements here. If you do not wish to add any to your thesis, you may simply add a blank titled Acknowledgements page.]

ABSTRACT

Multi-angle illumination-based computational microscopes have emerged as a promising class of imaging systems due to their capabilities and robustness across a wide range of applications, from biological imaging to materials inspection. In particular, quantitative phase imaging methods such as Fourier Ptychography Microscopy, Angular Ptychographic Imaging with Closed-form solutions and Kramers-Kronig relations leverage multi-angle illumination to surpass traditional space-bandwidth limitations and digitally correct aberrations. However, the performance of these systems is highly sensitive to misalignment in the illumination angles, and even minor perturbations can significantly degrade reconstruction quality and necessitate time-consuming recalibration. Thus, there is a pressing need for efficient and robust illumination angle calibration in such imaging modalities. We investigate how angular misalignments affect reconstruction fidelity and systematically evaluate a range of digital calibration strategies, including classical geometric models, cross-correlation-based methods, and learning-based approaches. These methods are benchmarked across varying signal levels and sample types. Our findings offer practical insights into selecting and deploying robust calibration techniques, ultimately supporting more resilient, reproducible, and high-throughput computational microscopy systems.

TABLE OF CONTENTS

LIST OF ILLUSTRATIONS

C h a p t e r   1

INTRODUCTION

1.1 Computational Imaging

Computational imaging refers to a class of imaging techniques that integrate physical imaging systems with algorithmic reconstruction to overcome the intrinsic limitations of conventional optics. Traditional imaging systems are constrained by physical limitations in optical design, such as the limited space-bandwidth product (SBP), and optical aberrations. These limitations present challenges for applications that demand both detailed structural information and large-area coverage, such as biological samples, semiconductor inspection, and materials analysis. By incorporating computational models into the image reconstruction process, these methods can synthetically increase resolution, correct for aberrations, and extract otherwise inaccessible information from raw intensity data.

A key subfield of computational imaging is quantitative phase imaging (QPI), which enables the recovery of a sample's complex optical field (amplitude and phase) from intensity-only measurements. This capability is particularly valuable for revealing intrinsic properties at the microscale, including those of biological specimens, microstructures, and engineered materials. Several QPI techniques have been developed to achieve this, including digital holography, coherent diffractive imaging (CDI), differential phase contrast (DPC), transport-of-intensity equation (TIE) methods, and FPM [1–6]. Among these, advanced methods such as FPM, Kramers-Kronig (KK) phase retrieval, and Angular Ptychographic Imaging with a Closed-form solution (APIC) stand out due to their ability to overcome the SBP, digitally correct for optical aberrations, and seamlessly integrate with LED-array microscope hardware [7].

1.2 Multi-angle illumination microscopy

To achieve those advantages, many QPI techniques leverage multi-angle illumination schemes, including FPM, APIC, and KK methods. These techniques capture and combine information from multiple illumination directions without any axial scanning, and they allow for the recovery of a broader range of the object's spatial frequencies. Multi-angle illumination can be realized through a variety of hardware configurations, such as a programmable LED array, galvanometric mirrors, a

digital micromirror device (DMD), or a spatial light modulator (SLM). The choice of illumination scheme depends on the imaging modality, sample type, and desired resolution or throughput. These methods have a wide range of applications, including cell biology, label-free live-sample imaging, digital pathology, and even non-destructive inspection of semiconductor devices.

1.3 Fourier Ptychography Microscopy

A notable method that relies on multi angled illumination is Fourier Ptychography Microscopy (FPM), which combines many low-resolution measurements to form a high-resolution image. FPM uses a programmable LED array to sequentially illuminate the sample from different angles. Each image captures a different band of spatial frequency content in the Fourier domain, and these low-resolution images are computationally stitched together to reconstruct a high-resolution complex field of the sample. This approach significantly extends the system's numerical aperture, yielding a higher-resolution, quantitative phase image without axial mechanical scanning. FPM also enables digital aberration correction and can be easily adapted to conventional microscope platforms, making it a flexible and powerful tool in biomedical imaging.
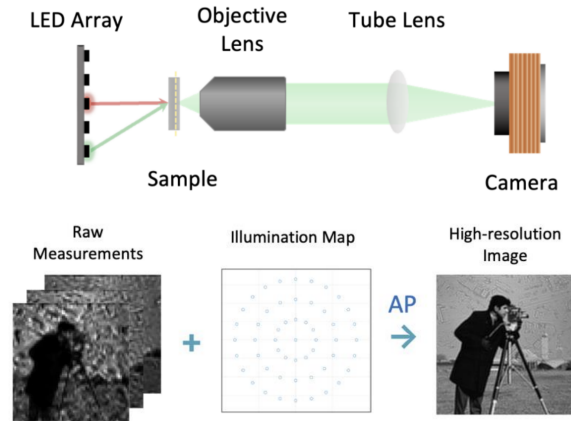
Figure 1.1: Overview of the FPM system and reconstruction pipeline. The setup consists of an LED array for multi-angle illumination, a standard 4f system with an objective and tube lens, and a camera for image acquisition. The LEDs provide a set of unique oblique illumination angle, producing a set of low-resolution measurements, as shown in the illumination map in spatial frequency space. These angles are used to computationally instruct iterative reconstruction of FPM high resolution images from the low-resolution measurements via an alternating projection (AP) algorithm.

1.4 Other angular illumination based imaging methods

Some other notable computational imaging techniques that also employ multi-angle illumination to enhance imaging capabilities include APIC, Structured Illumination Microscopy. One such method is Angular Ptychographic Imaging with Closed-form solutions (APIC), which, unlike FPM's iterative solvers, relies on NA-matching rings and analytical expressions to reconstruct the object's complex field, providing a fast and stable alternative for specific configurations [2]. Similarly, Structured Illumination Microscopy (SIM) uses patterned illumination, often generated using a spatial light modulator (SLM) or a digital micromirror device (DMD), to shift high-frequency object information into the passband of the microscope. DMD-based illumination systems, in particular, are capable of rapidly switching between illumination patterns, enabling high-speed acquisition and precise angular control [8].

In refractive index tomography [9, 10], angular scanning is typically achieved using galvanometric mirrors, which steer collimated beams across a range of incident angles. These systems enable volumetric reconstructions and three-dimensional imaging by combining multi-angle views with depth-resolved algorithms [11, 12].

Additionally, Kramers–Kronig (KK) phase retrieval has been adapted into angular-illumination-based setups where programmable illumination tiling improves spectral coverage and phase recovery. These illumination strategies enhance robustness and resolution without requiring mechanical scanning or complex optics. Across these techniques, angular diversity is a unifying mechanism that extends spatial frequency support, enables phase reconstruction, and facilitates computational aberration correction [13].

1.5 Illumination angle calibration

Despite the diverse range of applications and capabilities, all these techniques share a common challenge: accurate calibration of illumination angles. These systems are highly sensitive to misalignment, and even slight deviations such as bumping the optical setup or mechanical drifts over time can significantly degrade image quality, rendering the reconstructions unusable. Additionally, system modifications, such as switching to a different objective lens, necessitate recalibration, posing significant challenges for practical implementation. Thus, ensuring the reproducibility and accessibility of these image techniques necessitates the development of robust and efficient angle calibration strategies.
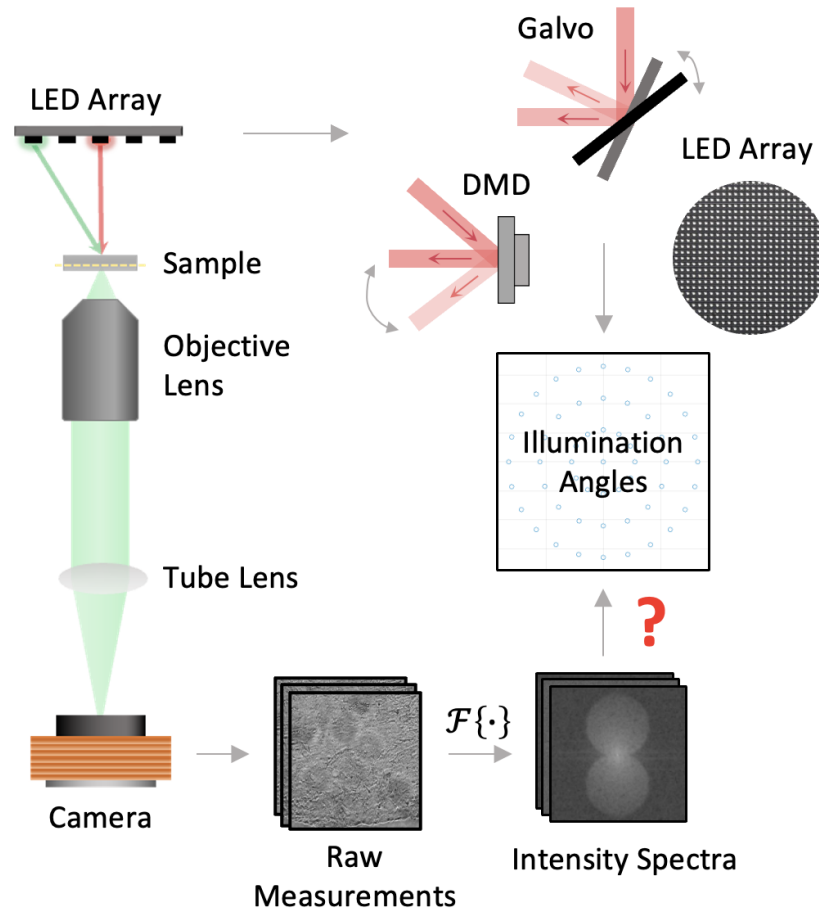
Figure 1.2: An illustration of the calibration scheme. On the left is a system that captures raw measurements illuminated at different angles. The illumination can be provided by a DMD, Galvo or an LED array. Each raw measurement has an intensity spectrum that corresponds to a unique illumination angle. Calibration aims to recover the correct illumination angles corresponding to each image for reconstruction usages.

Several approaches have been developed, ranging from mechanical pre-calibration methods to computational post-processing techniques. Mechanical alignment methods include precision LED array positioning and mirror-based localization, where markers or reflections are used to determine the exact illumination angles before imaging. While effective in controlled environments, these approaches often fail to correct dynamic misalignments that arise during long-term system operation.

To address these issues, simulated annealing-based methods such as SC-FPM, pcFPM, and mcFPM iteratively refine illumination positions by optimizing a misalignment correction term within the reconstruction pipeline [14–16]. These ap-

proaches are particularly useful for correcting global shifts rather than individual illumination angles, improving convergence speed by isolating parameter updates. Alternatively, cross-correlation-based methods leverage overlapping spectral information to refine illumination angles. The "Efficient Illumination Angle Self-Calibration" in FPM method [**11eckert2016algorithmic**] employs a two-step optimization approach, first estimating brightfield angles and then refining them iteratively using spectral correlations (BF-SC). Similarly, the translation position determination method integrates cross-correlation as a loss function within an optimization framework [17]. Machine learning (ML) based methods have also been explored, with Mask-RCNN-based calibration reformulating illumination estimation as an object detection problem in Fourier space. Deep learning approaches such as the Boundary Attention Method further enhance robustness in edge cases by refining angle predictions near object boundaries. While promising, these methods require extensive training datasets and may not generalize well across different experimental conditions [**14polansky2023boundary**, 18], Finally, vignetting-based correction techniques, such as LED Array Positional Misalignment Correction via Superimposed Images, overlay experimental and simulated images to estimate illumination shifts. These methods exploit center-region alignment and cross-correlation to improve calibration accuracy in non-uniform illumination conditions [19].

1.6   Roadmap

In this thesis, we demonstrated a generic robust calibration framework for multi-angle illumination microscopy. We systematically explore different methodologies for illumination angle calibration in FPM and related computational microscopy techniques. We discuss both hardware-based and post-acquisition computational calibration strategies, highlighting their trade-offs in terms of accuracy, robustness, and efficiency.

In section 2, we introduce the principals of FPM and derive the forward model of the system. In section 3, we demonstrate the effect of slight mismatches between the actual illumination angles and the illumination angles used for reconstruction. We simulate several scenarios that could cause such mismatches, including a deviation in height or lateral position, drifting over time, and random errors from DMDs or customized 3D printed systems. In section 4, we introduce the general calibration pipeline, and discuss some popular methods for calibration. In section 5, we focus on the cross-correlation term of the Fourier spectra of intensity measurements to digitally obtain illumination angles in a post-acquisition manner. In section 6,

we present experimental results, show how we can use the outlined methods for calibration, and bring in insights for sample selection and signal level adjustments for robust calibration settings.

Chapter 2

PRINCIPLES OF FPM

To investigate the effects of angular misalignment and evaluate calibration strategies, we focus our analysis on FPM as a case study for multi-angle illumination microscopes. FPM synthesizes a high-resolution image by stitching together multiple low-resolution intensity measurements acquired under different illumination angles. This illumination scheme is typically achieved using a programmable LED array, where each LED is sequentially lit up.

The illumination from a single LED can initially be modeled as a point source, emitting a spherical wave at a distance to the sample. Through free space propagation, the spherical wave gradually becomes a quasi-plane wave, according to the van Cittert Zernike theorem [20]. Within a small field-of-view, the quasi-plane wave can be considered as a coherent plane wave incident at some angle θ_i.

The sample $o(x, y)$ illuminated by an oblique plane wave incident at an angle θ_i can be modeled as

$$U_i(x, y) = o(x, y) \cdot \exp\left(j2\pi(k_{x,i}x + k_{y,i}y)\right) \tag{2.1}$$

where $i = 1, 2, 3, \ldots, n$ indicates the sequence number of the LED, U_i denotes the field at the sample plane, $k_{x,i}$ and $k_{y,i}$ denote the spatial frequency components in the x and y directions, respectively, given by $k_i = \frac{2\pi}{\lambda}\sin(\theta_i)$, where λ is the wavelength emitted by the LED.

The field then passes through the objective lens in the 4f system, which can be mathematically modeled as an optical Fourier transform

$$\mathcal{F}\{U_i(x, y)\} = O(k_x - k_{x,i}, \ k_y - k_{y,i}) \tag{2.2}$$

where $\mathcal{F}\{\ \}$ is the Fourier transform, $O(k_x, k_y) = \mathcal{F}\{o(x, y)\}$, and $k_{x,i}$ and $k_{y,i}$ correspond to shifts incurred by θ_i.

The pupil constraint of the objective lens acts as a low-pass filter and can be modeled by a coherent transfer function H

$$\Psi_i(k_x, k_y) = H(k_x, k_y) \cdot O(k_x - k_{x,i}, \ k_y - k_{y,i}) \tag{2.3}$$

where $\Psi_i(k_x, k_y)$ is the intermediate optical field at the pupil plane of the 4f system.

Then, the complex field passes through the tube lens of the 4f system

$$\psi_i(x, y) = \mathcal{F}^{-1}\left\{\Psi_i(k_x, k_y)\right\} \tag{2.4}$$

where $F^{-1}\{\ \}$ is the inverse Fourier transform, $\psi = \mathcal{F}^{-1}\{\Psi\}$

Finally, the measurement from angle θ_i illumination is formed and captured by the camera

$$I_i(x, y) = |\psi_i(x, y)|^2 \tag{2.5}$$

For simplicity, the general process of forward image formulation can be expressed as

$$I_i(x, y) = \left|\mathcal{F}^{-1}\left\{H(k_x, k_y) \cdot O(k_x - k_{x,i},\ k_y - k_{y,i})\right\}\right|^2 \tag{2.6}$$

This process is repeated across a series of LED positions, typically including several brightfield and some darkfield NA rings. Once all measurements are acquired, they are passed to a computational reconstruction algorithm that combines all the spectral information into a single high-resolution, quantitative phase image.

2.1 Theoretical representation of illumination angles in the spectral domain

In the reconstruction phase of FPM, all the low-resolution intensity measurements are combined to recover a high-resolution complex field of the sample through an iterative alternating projection algorithm. This algorithm alternates between the spatial and Fourier domains, updating the estimated object's phase and amplitude by enforcing consistency with the measured intensities. At each iteration, a portion of the Fourier domain is cropped based on the assumed illumination angle, propagated to the spatial domain, compared to the measured intensity, and then updated accordingly before returning to the frequency domain. Thus, to correctly stitch these measurements together, the reconstruction algorithm must accurately identify which region of the Fourier domain each image corresponds to.

This is typically estimated from the nominal LED angle using the relation

$$k_i = 2\pi \frac{\sin(\theta_i)}{\lambda} \tag{2.7}$$

where, as before, λ is the wavelength, θ_i is the incident illumination angle, and $o(x, y)$ denotes the object field.

However, if there are slight shifts in the system, the spectral regions will be incorrectly mapped, resulting in a faulty reconstruction.

If the incident wave has a perturbation $(\delta k_{x,i}, \delta k_{y,i})$, then from Eq. 1, the field can be expressed as

$$U_i(x, y) = o(x, y) \cdot \exp\left(j2\pi\left((k_{x,i} + \delta k_{x,i}) \cdot x + (k_{y,i} + \delta k_{y,i}) \cdot y\right)\right) \quad (2.8)$$

For slightly perturbed illumination angle $\theta' = \theta + \delta\theta$, the actual shift k'_i is

$$k'_i = 2\pi \frac{\sin(\theta_i + \delta\theta)}{\lambda} \quad (2.9)$$

We can simplify this with the first-order Taylor expansion

$$k'_i = 2\pi \frac{\sin(\theta_i) + \delta\theta \cdot \cos(\theta_i)}{\lambda} \quad (2.10)$$

Thus, the cropped spectral region will be erroneously shifted by the amount

$$\delta k_i = k'_i - k_i = 2\pi \frac{\delta\theta_i \cdot \cos(\theta_i)}{\lambda} \quad (2.11)$$

Plugging into (2.6), the actual measurement intensity will be shifted by the amount

$$I_i(x, y) = \left|\mathcal{F}^{-1}\left\{H(k_x, k_y) \cdot O(k_x - k_{x,i} - \delta k_{x,i}, \ k_y - k_{y,i} - \delta k_{y,i})\right\}\right|^2 \quad (2.12)$$
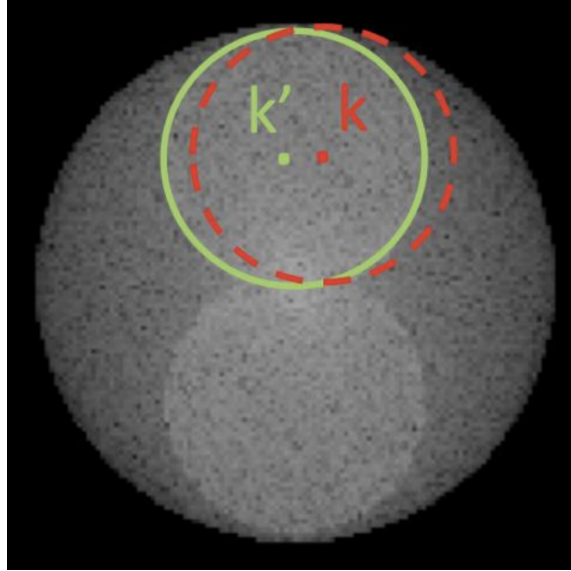
Figure 2.1: The effect of an illumination angle mismatch on the Fourier spectrum of a raw measurement. The actual (green) spectrum contains the frequency information of the intensity measurement, shifted by k'. However, our illumination angle map corresponds to the intended (red) spectra. Without calibration, the FPM reconstruction algorithm will end up using the red spectrum shifted by k.

Chapter 3

EFFECTS OF ILLUMINATION ANGLE MISMATCH

The slight mismatch in spectral shift has significant implications in terms of image quality. To quantify the impact of illumination angle misalignment on image reconstruction quality, we conducted controlled simulations of the FPM pipeline, introducing three distinct types of angular perturbations. These simulations were performed using Matlab's imaging library on two standard sample datasets, allowing for direct comparison of reconstruction quality under varying degrees of misalignment.

- **Random LED Jitter:** Each LED position was perturbed by a small, random displacement sampled from a uniform distribution, with a maximum deviation of one pixel. This simulates potential inconsistencies in LED array positioning due to fabrication errors or mechanical misalignment. These random mismatches could occur with DMDs, SLMs, or customized 3D printed domes, where individual pixels might have some mechanical or human error.

- **Global Shift:** A systematic translation was applied to all LEDs, shifting their positions by a uniform one-pixel displacement. This mimics errors arising from improper LED array alignment during setup, or from the system slightly drifting over time.

- **Height Mismatch:** A radial displacement was introduced to LED positions, mimicking misalignment due to incorrect LED array height relative to the sample plane. Such deviations lead to nonlinear illumination angle errors, significantly impacting high-frequency reconstruction accuracy. This is a more common alignment error, since the height is often manually adjusted.

The effects of illumination angle misalignment on FPM reconstruction quality were assessed by computing the peak signal-to-noise ratio (PSNR) of the reconstructed images relative to a ground truth reference, as outlined in Figures 3.1 and 3.2. To simulate the perturbations, we designed a forward model in MATLAB, based on the FPM formulation in Section 2. The illumination setup mimics a standard LED array system with a 10×, 0.25 NA objective lens and green light illumination from an LED

array. The samples imaged are constructed with example images from MATLAB's internal library. For FPM simulations, we use the "cameraman" figure for the amplitude and the "west concord orthophoto" for the phase. For APIC simulations, we use the "cell" figure for the amplitude and the "west concord orthophoto" for the phase. All images are typical benchmarking samples used by the computational imaging community. For each simulation, we generated low-resolution intensity measurements using shifted LED positions, then reconstructed the high-resolution complex object using an iterative alternating projection algorithm.

To model different system imperfections, we introduced random LED jitter, global shift, and height mismatch errors, as described above, in the illumination model. In the jitter condition, each LED's position was perturbed randomly in x and y, sampled from a uniform distribution with a maximum deviation of 3 pixels, corresponding to a few microns at the LED plane. For global shifts, we applied uniform displacement to all LED positions to simulate mounting misalignments or drift. For the height mismatch, the illumination angle was recalculated assuming incorrect vertical distance between the LED array and the sample, leading to non-uniform radial displacement in the spectrum.

Image Quality Quantification

Misalighment vs PSNR

Figure 3.1: Quantification of the effect of misalignment. The PSNR of the image is plotted against the LED misalignment, measured by the mean squared error in k space. There is a noticeably sharp initial decline in image quality for a slight misalignment. For a total shift in illumination accuracy of 0.015 (in k space), which corresponds to a < 0.2 cm shift of the LED, the image quality degrades by up to 10 dB.
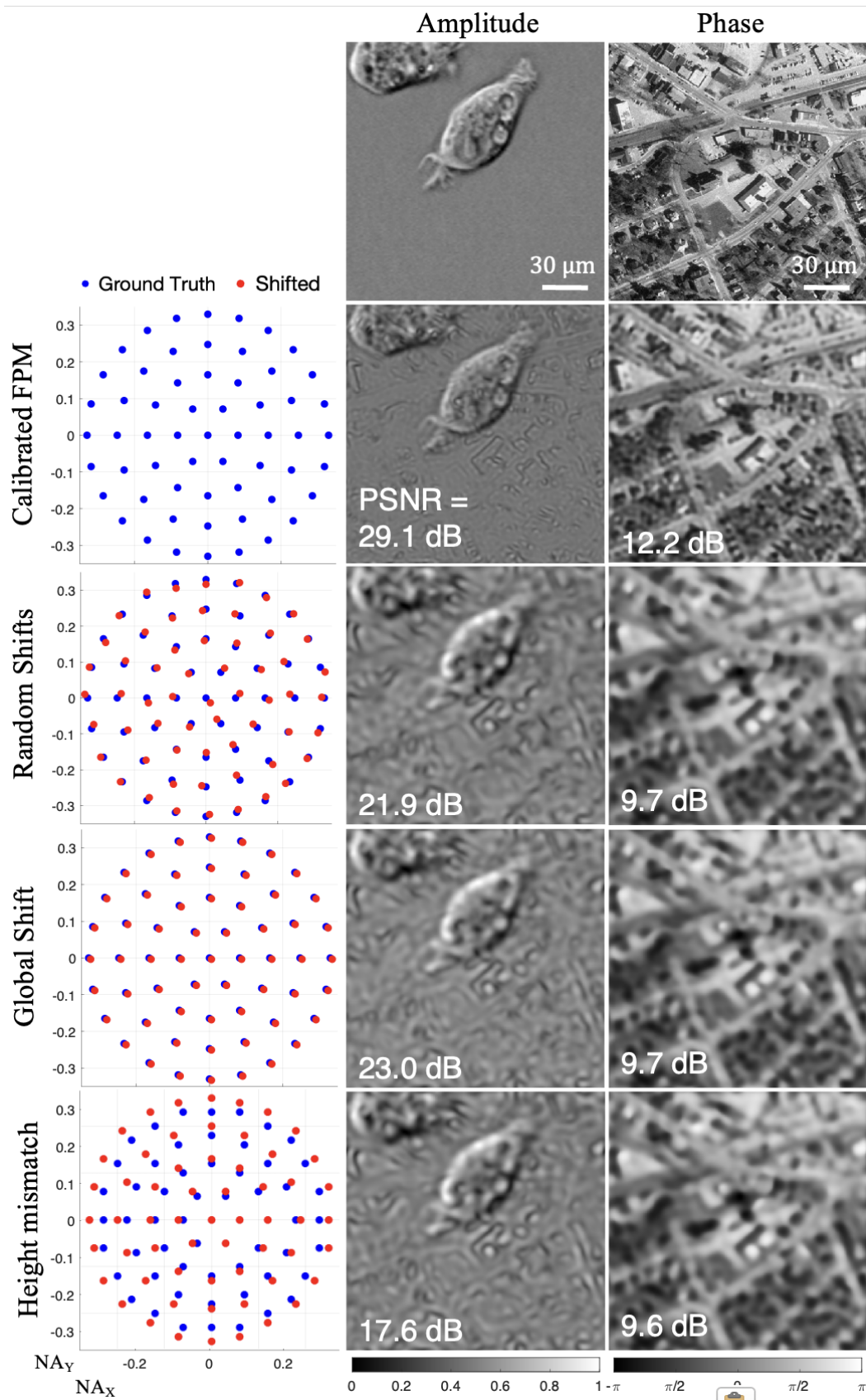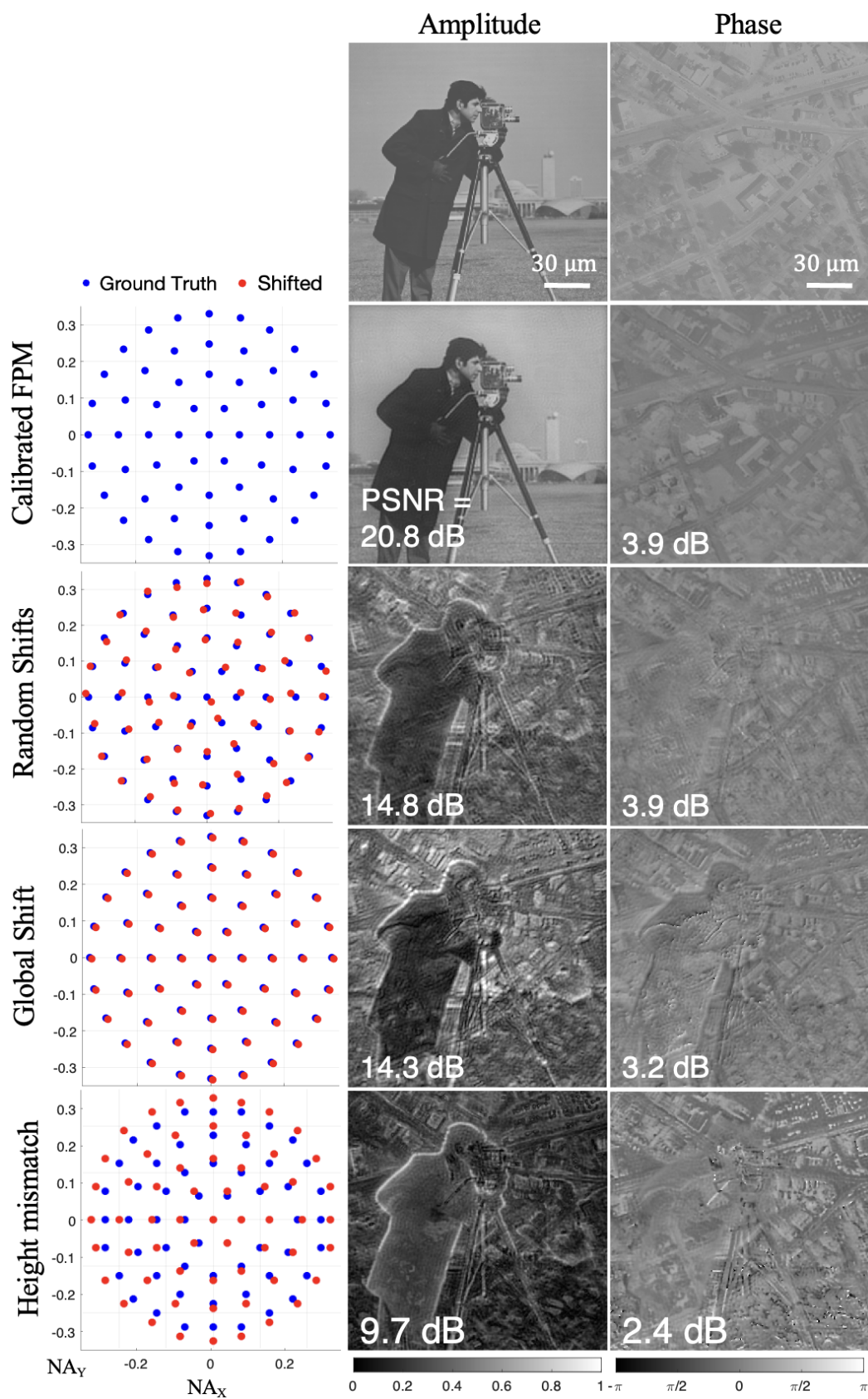
Figure 3.2: Impact of illumination angle misalignment on FPM (top) and APIC (bottom) reconstruction quality. Each row represents a different perturbation scenario applied to the illumination angles; from top to bottom, calibrated FPM (reconstruction with no mismatch), random shifts, global shift and height mismatch. The left column shows the illumination angle maps, with blue dots representing the ground truth positions (used in reconstruction) and red dots indicating perturbed angles (used for illumination). The middle column displays the reconstructed amplitude images, and the right column shows the corresponding phase reconstructions. Each reconstruction is paired with a peak signal-to-noise ratio (PSNR) value measuring fidelity against a ground truth reference.

Each reconstructed image was compared against the ideal reconstruction, with no illumination angle misalignments, using PSNR. As shown in Figure 3.1, image quality degrades noticeably even for small misalignments: PSNR drops by over 10 dB as the mean squared shift increases from zero to just 3 pixels, which corresponds to an LED displacement of < 3 um. The degradation sharply declines after a small threshold, which further underscores the high sensitivity to slight perturbations. In the FPM and APIC examples (Figure 3.2), the reconstructions exhibit loss of high-frequency detail and increased artifacts.

This behavior reflects the high sensitivity of such imaging methods on accurate illumination angle calibration. Because each LED illumination contributes new information to specific bands of spatial frequencies, any shift in the estimated angle misplaces those frequency components, leading to incorrect spectrum stitching and phase reconstruction. The resulting artifacts are particularly pronounced in the high-frequency regime, as seen in the FPM and APIC examples (Figure 5bc), where edge sharpness is lost, and fine structural features become distorted or aliased.

These findings highlight the sensitivity of FPM and APIC to illumination angle accuracy; even small misalignments in illumination geometry can significantly degrade reconstruction quality. We showed that illumination angle misalignment significantly degrades image quality, even when all other system parameters are ideal. Thus, it is evident that mechanical setup alone is insufficient to ensure reliable performance, and robust digital calibration procedures must be integrated into the imaging pipeline to dynamically estimate and correct angular errors. This need becomes even more critical in systems using DMDs, galvo mirrors, or large-area LED arrays, where alignment variation can be systematic or spatially non-uniform. Our demonstration strongly motivates the development of robust, accurate, and practical calibration methods, which we address in the next section.

Chapter 4

GENERAL CALIBRATION PIPELINE

As shown, accurate calibration is essential to ensure the fidelity of reconstructions in multi-angle illumination-based computational microscopy systems such as FPM and APIC. Calibration typically begins with mechanical alignment during the initial assembly or reconfiguration of the system. This involves physically aligning the LED array, adjusting the sample height, centering the objective, and ensuring that the optical components are positioned according to the design specifications. These mechanical steps are essential for establishing a baseline alignment, especially when the system is first installed or after major hardware changes, such as switching objectives or repositioning the sample stage.

After the initial setup, frequent mechanical adjustments are typically unnecessary, since once the system is aligned, we can rely on digital calibration methods to more precisely fine-tune and maintain performance over time. Digital calibration can estimate and correct residual misalignments in the illumination angle model, compensate for sample tilts, and perform aberration correction. This digital step of calibration significantly reduces the need for repeated manual tuning and supports consistent performance across experiments. It also enhances the system's usability and robustness, making computational microscopy platforms more adaptable to non-expert users and better suited for commercial, clinical, or field deployment. This general pipeline is illustrated in Figure 4.1.
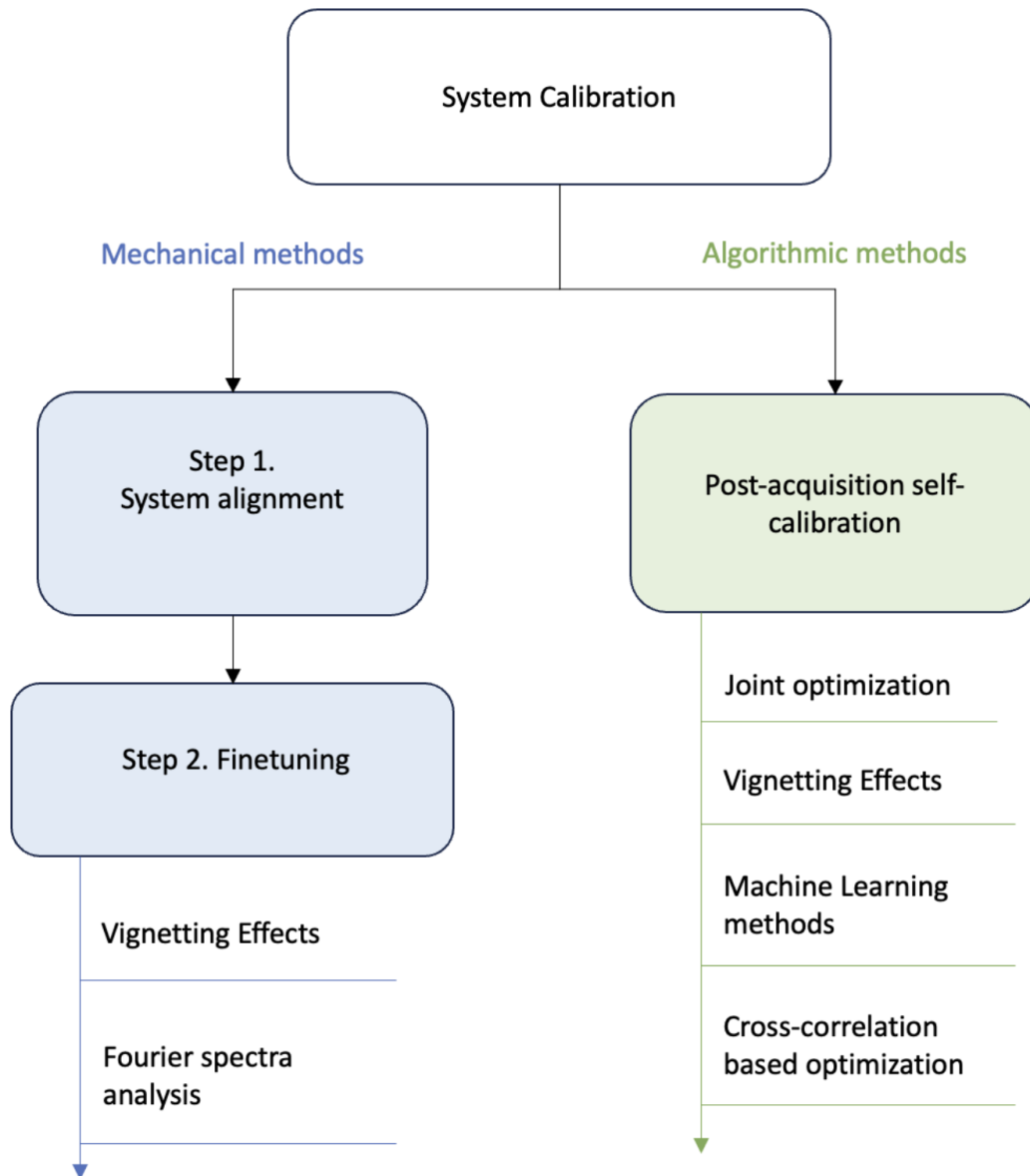
Figure 4.1: A flowchart representing the general calibration pipeline. The calibration process can be broadly divided into two categories: mechanical methods (left) and algorithmic methods (right). Mechanical calibration begins with coarse system alignment followed by fine-tuning procedures that may include inspection of vignetting effects or Fourier spectrum analysis. Algorithmic calibration refers to calibration that no longer has access to the system hardware and is performed post-acquisition. It includes methods such as joint optimization during image reconstruction, analysis of vignetting effects, machine learning based calibration methods, and cross-correlation term analysis.

There are several methods for digital calibration. One class of methods focuses

on joint optimization, such as such as SC-FPM, pcFPM, and mcFPM, in which both the sample field and illumination angles are iteratively refined within the reconstruction loop. This is accomplished by refining angle estimates by minimizing a misalignment-dependent error term, often via simulated annealing algorithms [14–16]. These methods are particularly effective for correcting global shifts across the LED array and optimizing system-wide calibration with fewer assumptions about individual angles. Their main limitation is the computational cost and convergence guarantee, especially for systems with larger misalignments or many illumination angles.

Another method introduces vignetting effects into a superimposed image alignment algorithm (SIA). The vignetting effect is a natural intensity fall-off toward the edges of images caused by angular illumination. The SIA overlays simulated and experimental low-resolution images to iteratively estimate the illumination angles that best explain the observed vignetting patterns [19]. By optimizing the similarity between experimental and simulated vignetting profiles using normalized cross-correlation, the method can recover sub-pixel corrections without any hardware changes. This approach is highly precise, however, its accuracy is highly dependent on the sample being centrally located and relatively uniform, as strong object features may confound the vignetting pattern. Additionally, it assumes consistent illumination intensity across LEDs and uniform sample scattering, which may not hold in all scenarios.

Recently, machine learning methods have also emerged. These approaches reformulate angle calibration as a data-driven inference task and train deep convolutional neural networks trained to predict illumination positions from Fourier-domain intensity patterns, usually through segmentation. One notable example is the Mask R-CNN–based calibration framework, which treats angle estimation as an object detection problem in Fourier space. [18] The primary advantage of ML approaches is their speed, scalability, and robustness to noise and sample variation. Once trained, these models can infer angle shifts rapidly and consistently across diverse imaging conditions. However, it is challenging to create representative training datasets that can generalize to unseen experimental settings. Additionally, these models can be rather computationally expensive to train. ML approaches are especially useful for large illumination schemes, such as 3D FPM, since it allows for batchwise operations that quickly calibrate a large group of illumination angles at once.

Lastly, of the many methods for calibration, another common and robust one is to

look at the cross-correlation term of the Fourier transform of the intensity measurements, which we will focus on in the next section. The underlying idea is that by identifying and cropping the relevant sections in the Fourier domain, which correspond to shifted replicas of the object spectrum, we can estimate the spatial frequency shift. These shifts can then be directly mapped to the corresponding illumination angles using a simple geometric relationship. As a result, the cross-correlation term can be accessed directly by applying a Fourier transform to the low-resolution intensity measurement, which makes this a fast, accurate, and accessible means for digital calibration.

C h a p t e r 5

DIGITAL CALIBRATION USING CROSS-CORRELATION

To understand the origin of the cross-correlation term in the intensity spectrum, we begin by analyzing a single low-resolution measurement taken under oblique illumination. First, consider a Fourier transform to the low-resolution intensity measurement. The resulting Fourier spectrum contains distinct features, including central autocorrelation lobes and sidebands arising from interference between the object and the background (or DC) term. These cross-correlation sidebands appear symmetrically offset from the center and encode the shift of the object's spectrum due to oblique illumination.

Recall from (2.5) that a low-resolution measurement can be expressed as

$$I_i(x, y) = |\psi_i(x, y)|^2 \tag{5.1}$$

where

$$\psi_i(x, y) = \mathcal{F}^{-1}\left\{H(k) \cdot O(k - k_i)\right\} \tag{5.2}$$

The sample $o(x, y)$ can be expressed as a summation of two terms: the scattered sample o_s and the DC component r, so we can write

$$\psi_i(x, y) = \mathcal{F}^{-1}\left\{H(k) \cdot \mathcal{F}\{o_s + r\}\right\} \tag{5.3}$$

Since r is the DC component of o,

$$H(k) \cdot \mathcal{F}\{r\} = \delta(k - k_i) \tag{5.4}$$

where $\delta(k)$ is the dirac delta function

For simplicity, since $H(k)$ acts as a low-pass filter, let us define

$$OS_L = H(k) \cdot \mathcal{F}\{o_s\} \tag{5.5}$$

With (5.4) and (5.5), we can express ψ_i as

$$\psi_i(x, y) = \mathcal{F}^{-1}\{OS_L + \delta(k - k_i)\} \tag{5.6}$$

Now, to access the Fourier spectrum of the low-resolution measurement I_i, we take the Fourier transform

$$\mathcal{F}\{I_s(x, y)\} = \mathcal{F}\left\{\left|\mathcal{F}^{-1}\{OS_L + \delta(k - k_i)\}\right|^2\right\} \tag{5.7}$$

By the convolution theorem,

$$\mathcal{F}\{I_s(x, y)\} = (OS_L + \delta)^* * (OS_L + \delta) \tag{5.8}$$

Thus, the Fourier spectrum can be expressed as

$$\mathcal{F}\{I_s(x, y)\} = OS_L^* * \delta(k - k_i) + OS_L * \delta^*(k - k_i) + OS_L^* * OS_L + \delta \tag{5.9}$$

$\mathcal{F}\{I_s(x, y)\}$ contains two cross-correlation terms and two autocorrelation terms. The former corresponds to the smaller circles in Figure 5.1 that are symmetrically shifted. The latter corresponds to the large outer circle.
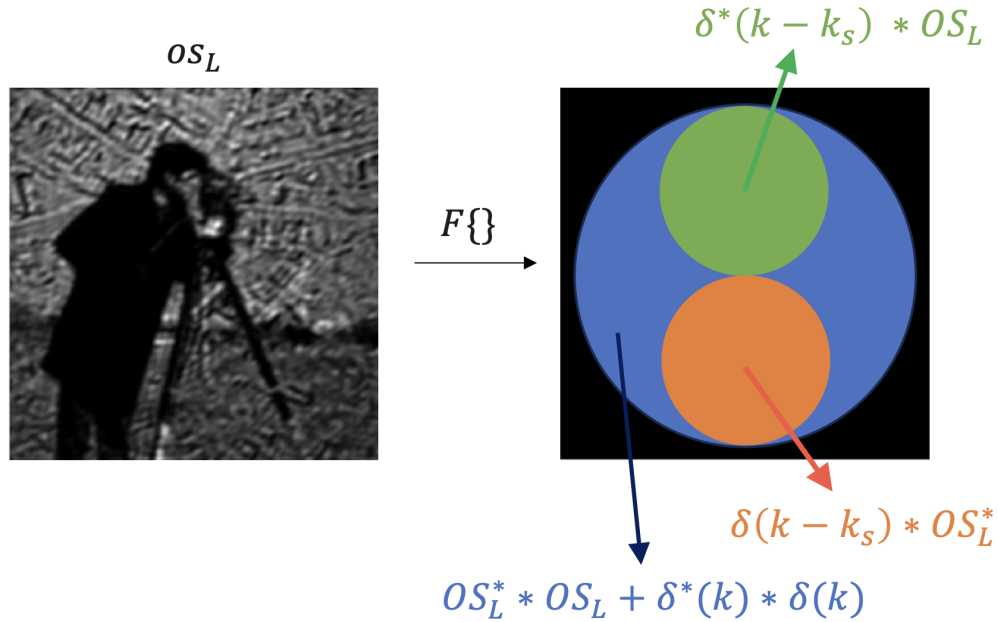
Figure 5.1: A breakdown of the Fourier intensity spectra of a low-resolution measurement. On the left is an object illuminated from an angle. On the right is its corresponding Fourier spectra, $\mathcal{F}\{OS_L\}$, which has multiple terms. The autocorrelation terms $OS_L^* * \delta(k - k_i) + OS_L * \delta^*(k - k_i)$, shown in blue, make up the central region and appears as a large circle. The cross-correlation terms, $OS_L^* * OS_L + \delta$, shown in orange and green, appear as the two shifted smaller circles, and are located symmetrically about the center at positions determined by the illumination angle.

Now, since these cross-correlation terms encode the spatial frequency shift intro-
duced by the illumination angle, we can work backwards from the cross-correlation
term to infer the illumination angle.

Rearranging (2.7), we can express θ_i as

$$\theta = \sin^{-1}\left(\frac{\lambda k_i}{2\pi}\right) \tag{5.10}$$

Thus, by detecting the position of the smaller circles, we can quantify the spectrum
shift k_i and directly calculate the illumination angle θ_i. However, this formulation
assumes the presence of a DC term in the sample, which corresponds to a weakly
absorptive object. For strongly absorptive samples, the delta function representation
breaks down, and the cross-correlation term in Eq. (5.9) will not be valid.

Chapter 6

METHODS FOR ILLUMINATION ANGLE CALIBRATION

Having established how we can identify the true illumination angle by segmenting the cross-correlation term, we now demonstrate how this method can be applied in practice. This section presents an experimental evaluation of three calibration strategies: a classical circle detection method (Hough transform), a recent iterative algorithm (BF-SC), and a ML-based method using boundary attention models. We test across varying signal levels and sample conditions to assess their performance, robustness, and failure modes.

In our experiments, we first collect a batch of low-resolution images illuminated from different angles. Then, we apply the calibration method to the image stack. Each method segments the low-resolution image's Fourier spectra to identify the LED locations. Then, the LED locations can simply be passed to the reconstruction algorithm. This pipeline is outlined in Figure 6.1.

It is important to acknowledge that calibration methods are also influenced by the sample being imaged and the overall signal level. Certain samples, such as those with fine structural details or strong phase contrast, exhibit a full spectrum, which ensures better convergence in calibration algorithms. In contrast, weakly scattering or low-contrast samples, such as thin biological specimens, can pose challenges due scattering or limited frequency information available in their Fourier spectra. They may not produce strong or well-defined circles, making it more difficult to estimate the spectrum's shift and thereby the illumination angle. Additionally, low signal-to-noise ratio (SNR) settings reduce the system's ability to capture and preserve high-frequency features, which make calibration difficult for similar reasons. The effects are shown in the bottom row of Figure 6.1. In our experiments, we selected a sample with well-defined cross-correlation features to better outline the effects of signal level.
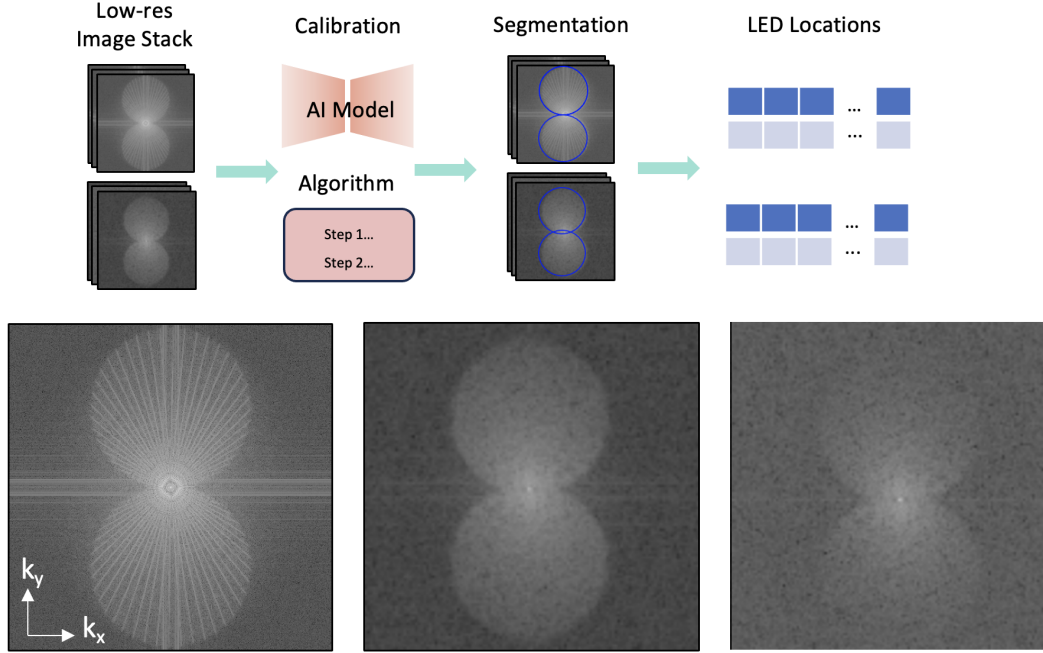
Figure 6.1: Calibration pipeline and sample selection. The top row depicts an overview of the calibration pipeline based on the cross-correlation term. The Fourier spectra of a stack of low-resolution measurements is passed through some calibration method, which may use either an AI-based model or a classical algorithm. This process identifies the location of the spectral shift in each image through segmentation, which we can then use to estimate LED illumination angles. Thus, we have a stack of calibrated LED positions. The bottom row depicts some examples of Fourier intensity spectra from three different samples, illustrating variability in spectral features due to differences in structure, signal level and scattering properties. Such variation impacts the clarity of the cross-correlation terms and, consequently, the performance of calibration methods.

6.1 Benchmark Calibration Algorithms

We compare several algorithms against each other. The first benchmark method we use is a classical circle detection method called the Hough transform. This is a feature detection algorithm that detects edges through a voting scheme in the parameter space (a, b, r), where (a, b) is a potential center and r is a potential radius [21, 22]. It is computationally efficient and simple to implement but is sensitive to noise and can thus be unreliable.

The second benchmark method we evaluate against is an efficient self-calibration algorithm that iteratively estimating initial LED illumination positions based on rough geometric alignment or brightfield estimates and then refines them by leveraging the redundancy in overlapping Fourier spectra using spectral correlations (BF-SC).

In each iteration, the algorithm compares simulated and measured spectral shifts to update LED positions. It is robust to moderate noise and structural variation in the sample but is computationally more expensive and specific to FPM [21].

The third benchmark method we use is a machine learning-based algorithm that we designed, inspired by the Boundary Attention (BDA) network architecture originally developed for robust segmentation in noisy and low-contrast imaging scenarios. [**14polansky2023boundary**] Our method applies the BDA network to segment the cross-correlation regions in the Fourier spectra. After segmentation, we perform circle fitting on the three strongest detected edge points, as determined by a combination of edge confidence from the BDA output and proximity to a rough geometric prior based on the known LED array layout. This approach is designed to not only be more robust across a range of sample types and signal levels but also be less computationally intensive due to the batch processing abilities in machine learning. Thus, it can scale up to 3D FPM or larger illumination schemes with ease.

6.2 FPM Experimental Setup

We show experimental results from a conventional FPM system with an objective lens (Olympus PLAN 10x/0.25NA), at 520 nm wavelength from green LEDs (Adafruit Inc. 5050 RGB LED). The illumination was provided by an LED array controlled via an Arduino Uno board. A human breast cancer with HER2 mutation sample was imaged. We achieved variations in SNR by sweeping through different exposure levels (16 values between 500 ms to 5 s) and capturing a full set of images for each value. Then, we compared the LED location accuracy between the three calibration algorithms for each image set.

For each exposure level, a full set of raw images was captured and processed independently through each calibration method. The performance of each algorithm was evaluated by measuring the mean squared error of estimated illumination angles from a high-SNR ground truth. To quantify the sample's ease of angle-identification, we computed the power density of the sample spectra. We opted for this metric in order to provide an interpretable measure of the visibility and sharpness of cross-correlation features in the Fourier domain. Moderate power density (between approximately 0.01 and 0.5) indicates broader and more distinguishable spectral components, enabling more accurate calibration. High power density (> 0.5) indicates that the Fourier spectrum is centered around the DC region and thus may not be fully complete. Examples of each case are shown in Figure 10. Lower power

density (<0.01) corresponds to samples that are overexposed and thus have smaller average signal values due to increased scattering.

6.3   Results

Our experimental design allowed us to directly compare the sensitivity of each method to noise and isolate failure modes. The results are summarized in Figure 6.2.
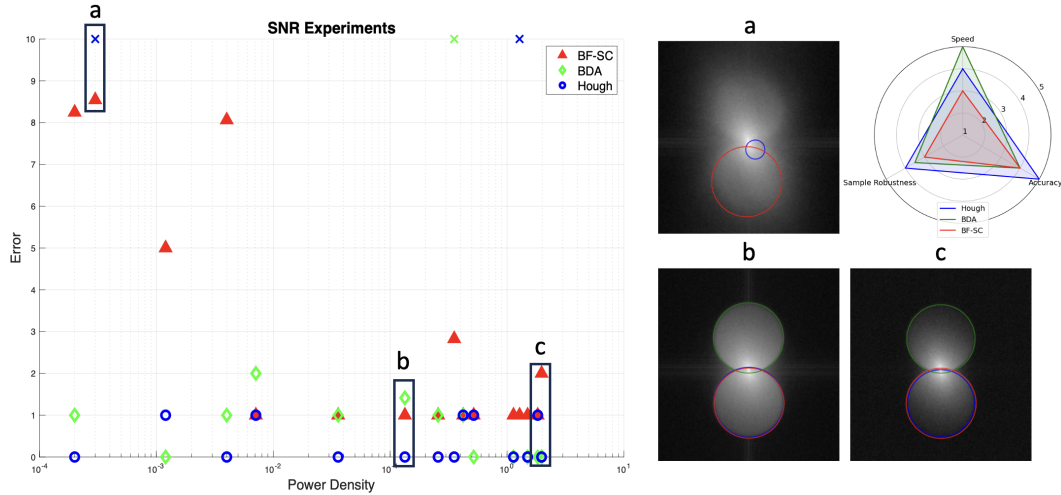

Figure 6.2: Comparison of calibration methods across SNR conditions. The left side depicts the calibration error plotted as a function of spectra power density for each of the three methods: the Hough transform-based method (blue), efficient algorithmic self-calibration (red), and a machine learning-based approach (green). Data points marked with "x" indicate large errors (>10) or cases in which the algorithm fails to identify a boundary. We observe that the machine learning method maintains consistently low error across all SNR levels, but struggles to segment some samples, the iterative method fails under low-SNR conditions, and the Hough method struggles with ambiguous features. The right side depicts example spectra and their corresponding segmentations by each method at three selected points (a, b, c) on the graph. The top right depicts a radar plot summarizing a rough qualitative comparison of the three methods across speed, accuracy, and robustness to sample variation.

From our results, it's evident that the SNR of the system can significantly degrade calibration accuracy. When the Fourier spectrum is sufficiently rich and well-defined across spatial frequencies, which corresponds to moderate power densities, all three calibration methods perform well and typically localize LED shifts within 1–2 pixels. The Hough and BF-SC methods have the most consistently low error; both rely on algorithmic optimization rather than learned/data-driven behavior, which makes

their performance stable under suitable conditions. The former uses a deterministic algorithm for detecting circular features, and thus will work reliably when circle-like structures are clearly visible in the Fourier domain. Similarly, since BF-SC leverages overlapping spectral content and geometric constraints, it is also quite accurate when the input data is clean. While the BDA method performs well in these conditions, it has slight sensitivity to spectral edge ambiguity due to its tendency to overemphasize strong boundary signals, which can cause it to misidentify edges. In terms of speed, the BDA method and the Hough transform have the fastest performance, operating on the order of milliseconds per frame. BF-SC, being an iterative method with global optimization steps, typically takes several seconds per frame, making it less suitable for real-time applications but more reliable in complex scenarios

As the power density increases further, the spectra tend to collapse toward the DC region. This trend is indicative of lower SNR conditions and results in poorly defined circles, as the higher frequencies may blend in with the system noise, as can be seen in example (c) of Figure 10. Under these conditions, the BF-SC method begins to show notable limitations. Its brightfield–darkfield classification step often mislabels weak brightfield measurements as darkfield, and will fail to calibrate the measurement. Furthermore, because the high-frequency edge of the spectrum becomes incomplete or blurred, the spectral correlation step slightly loses precision, leading to calibration errors of up to 3 pixels. In contrast, the Hough transform method continues to stay within the 1 to 2 pixel margin, likely due to its voting-based framework, which aggregates information from individual edge pixels across the spectrum. This allows it to detect circles even when the boundary is incomplete or blurred, as it can leverage localized segments of the spectrum to infer the overall circular geometry. The BDA method also demonstrates strong robustness, as its segmentation strategy focuses only on the three strongest points of the spectrum boundary. In low SNR cases, it can prioritize points closer to the DC term, allowing it to remain effective even when peripheral features are less identifiable. However, this also makes it more susceptible to failure. If it identifies a strong edge that is not on the circle boundary, it will completely misidentify the spectrum shift.

For lower power densities, which correspond to samples with excessive scattering, or other features that blur the boundaries of the cross-correlation lobes, all three methods become less reliable. In these cases, the circle boundaries are weak or ambiguous, making accurate segmentation difficult. The Hough transform and

BDA methods can often still produce estimates within 1–2 pixels of the ground truth, but this apparent success is largely attributable to strong priors, rather than accurate extraction of spectral features. In low-SNR or heavily blurred conditions, the calibration algorithm lacks sufficient signal to make a confident inference and instead defaults to prior expectations. The BF-SC method is particularly vulnerable, with average errors of around 7 pixels. Because its optimization process relies on accurate correlation between overlapping spectral regions, inconsistently blurred spectral boundaries might mislead the update direction and cause it to converge to a local minimum. However, as shown in example (a) of Figure 10, all three methods are prone to outright failure when the signal quality falls below a critical threshold.

6.4 Discussion

Between the three calibration methods evaluated, each presents distinct strengths and limitations depending on the sample characteristics and signal conditions. For samples with abundant frequency information, strong SNR, and thus reasonably well-defined spectrum boundaries, the Hough circle transform is the most efficient and accurate algorithm. For these samples, if computation time is critical, the BDA method is also a great option. It performs reliably and can calibrate a large number of LEDs at once, thanks to ML batch processing abilities. For samples with slightly weaker high-frequency features, the BF-SC and Hough methods demonstrate the best performance. For samples with strong scattering, the Hough and BDA methods are optimal.

In terms of methods, each has its own advantages and disadvantages. The Hough circle transform is accurate and efficient but is susceptible to scattering samples. The BDA method is robust to situations where the high frequency components are weaker, and can batch process, but has a higher likelihood of failing to calibrate. The BF-SC method is accurate, but slower than the other two and more susceptible to samples that do not have clearly defined spectra.

Thus, our experiments reveal clear tradeoffs between simplicity, robustness, and generalizability across classical, algorithmic, and learning-based methods. In particular, calibration accuracy is highly dependent on the sample's spectral richness and the signal-to-noise regime. These insights underscore the need for adaptive and context-aware calibration pipelines. Future work may explore hybrid calibration schemes, integrate novel image processing advancements, and leverage machine learning frameworks to further enhance robustness and scalability.

Chapter 7

CONCLUSION

Overall, in this thesis, we investigated the methods of illumination angle calibration in multi-angle illumination-based imaging systems, with a particular focus on FPM. These imaging methods offer significant advantages, such as digital aberration correction and overcoming the SBP but are critically sensitive to angular misalignments. We demonstrated how small deviations that shift the spectrum by up to 3 pixels can lead to substantial degradation (up to 10 dB in PSNR) in reconstruction quality. To address this challenge, we presented a comprehensive illumination angle calibration framework and benchmarked different methods (Hough transform, BF-SC, BDA algorithm) under varying signal levels and sample types, highlighting trade-offs between speed, sample robustness, and accuracy. We found that the sample characteristics and system SNR can significantly affect the success of illumination angle calibration. By characterizing the strengths and limitations of different approaches under real-world conditions, this thesis provides a framework for understanding and improving angle calibration in computational microscopy, and it offers practical guidance for selecting or designing calibration pipelines that suit specific applications.

Ultimately, improving the efficiency and robustness of illumination angle calibration contributes to the broader goal of making computational microscopy more practically accessible, including in applications such as live-cell imaging, digital pathology, and materials characterization. However, while the three methods have different advantages and disadvantages, there are scenarios where they all become unreliable, such as when there is excessive scattering or when the sample is overexposed. Thus, there is a pressing need for more adaptive and intelligent illumination angle calibration algorithms that can operate reliably across a broader range of sample conditions. Future work could explore hybrid approaches that combine geometric priors with learned features. It would be interesting to take advantage of recent advancements in computer vision and image processing to develop a more targeted illumination angle calibration algorithm for example, a novel boundary detection ML algorithm could be trained with optimization methods used in BF-SC by introducing a spectral correlation term into the loss function of the ML training process. This would also make the ML model self-supervised, which would alle-

viate concerns about out-of-distribution generalization. Additionally, an extensive pretraining process would no longer be necessary.

BIBLIOGRAPHY

[1] Guoan Zheng, Roarke Horstmeyer, and Changhuei Yang. "Wide-field, high-resolution Fourier ptychographic microscopy". In: *Nature photonics* 7.9 (2013), pp. 739–745.

[2] Ruizhi Cao, Cheng Shen, and Changhuei Yang. "High-resolution, large field-of-view label-free imaging via aberration-corrected, closed-form complex field reconstruction". In: *Nature Communications* 15.1 (2024), p. 4713.

[3] Zhaohui Huang and Lin Cao. "Quantitative phase imaging based on holography: trends and new perspectives". In: *Light: Science & Applications* 13.1 (2024), p. 145.

[4] Etienne Cuche, Pierre Marquet, and Christian Depeursinge. "Spatial filtering for zero-order and twin-image elimination in digital off-axis holography". In: *Applied optics* 39.23 (2000), pp. 4070–4075.

[5] Jianwei Miao et al. "Extending the methodology of X-ray crystallography to allow imaging of micrometre-sized non-crystalline specimens". In: *Nature* 400 (1999), pp. 342–344.

[6] Shalin B Mehta and Colin JR Sheppard. "Quantitative phase-gradient imaging at high resolution with asymmetric illumination-based differential phase contrast". In: *Optics letters* 34.13 (2009), pp. 1924–1926.

[7] Cheng Shen et al. "Non-iterative complex wave-field reconstruction based on Kramers–Kronig relations". In: *Photonics Research* 9.6 (2021), pp. 1003–1012.

[8] Manish Saxena, Gangadhar Eluru, and Sai Siva Gorthi. "Structured illumination microscopy". In: *Advances in Optics and Photonics* 7.4 (2015), pp. 241–275.

[9] Ruilong Ling et al. "High-throughput intensity diffraction tomography with a computational microscope". In: *Biomedical Optics Express* 9.5 (2018), pp. 2130–2141.

[10] Zhenyu Dong et al. "Analytic Fourier ptychotomography for volumetric refractive index imaging". In: *https://arxiv.org/abs/2504.16247* (2025).

[11] Marc Levoy et al. "Light field microscopy". In: *ACM Transactions on Graphics (TOG)* 25.3 (2006), pp. 924–934.

[12] Di Jin et al. "Tomographic phase microscopy: principles and applications in bioimaging". In: *Journal of the Optical Society of America B* 34.5 (2017), B64–B77.

[13] Yiran Wang et al. "Structured illumination microscopy based on Kramers–Kronig relations for quantitative phase reconstruction". In: *Optics Letters* 49.24 (2024), pp. 6801–6804.

[14] A Pan et al. "System calibration method for Fourier ptychographic microscopy". In: *Journal of Biomedical Optics* 22.9 (2017), p. 096005. DOI: `10.1117/1.JBO.22.9.096005`.

[15] Hao Wei et al. "Accurate and stable two-step LED position calibration method for Fourier ptychographic microscopy". In: *Journal of Biomedical Optics* 26.10 (2021), p. 106003.

[16] Ao Zhou et al. "Fast and robust misalignment correction of Fourier ptychographic microscopy for full field of view reconstruction". In: *Optics express* 26.18 (2018), pp. 23661–23674.

[17] Fucai Zhang et al. "Translation position determination in ptychographic coherent diffraction imaging". In: *Optics express* 21.11 (2013), pp. 13592–13606.

[18] Florian Ströhl et al. "Object detection neural network improves Fourier ptychography reconstruction". In: *Optics express* 28.25 (2020), pp. 37199–37208.

[19] Houliang He et al. "LED array positional misalignment correction method based on superimposed images for Fourier ptychography". In: *Optics Express* 33.4 (2025), pp. 7492–7507.

[20] Max Born et al. *Principles of Optics: Electromagnetic Theory of Propagation, Interference and Diffraction of Light*. 7th. Cambridge University Press, 1999.

[21] Regina Eckert. "Robust 3D Quantitative Phase Imaging". PhD Thesis. EECS Department, 2022.

[22] H.K. Yuen et al. "A comparative study of Hough transform methods for circle finding". In: *Proc. 5th Alvey Vision Conference*. 1989, pp. 169–174.